Korean J. Chem. Eng., 38(2), 292-305 (2021)
DOI: 10.1007/s11814-020-0675-2

pISSN: 0256-1115
eISSN: 1975-7220

Effects of catalysts on structural and adsorptive properties of iron oxide-silica nanocomposites

Cătălin Ianăşi*, Paula Ianăşi (b. Svera),***, Adina Negrea****,†, Mihaela Ciopec****, Oleksandr I. Ivankov*****,******,*******, Alexander I. Kuklin*****,******, László Almásy********, and Ana-Maria Putz*,†**

*"Coriolan Drăgulescu" Institute of Chemistry, 24th Mihai Viteazul Bvd., 300223, Timişoara, România
**National Institute for Research and Development in Electrochemistry and Condensed Matter, 144th Prof. Dr. Aurel Paunescu-Podeanu Street, 300569, Timişoara, România
***Department of Biology-Chemistry, Faculty of Chemistry, Biology, Geography, West University of Timişoara, Pestalozzi Str. No. 16, RO-300115, Timişoara, România
****Politechnica University of Timişoara, Faculty of Industrial Chemistry and Environmental Engineering, 6th Vasile Pârvan Bvd., 300223, Timişoara, România
*****Frank Laboratory of Neutron Physics, Joint Institute for Nuclear Research, Joliot-Curie 6, Dubna, Russia
******Research Center for Molecular Mechanisms of Aging and Age-Related Diseases, Moscow Institute of Physics and Technology, 141701 Dolgoprudny, Russia
*******Institute for Safety Problems of Nuclear Power Plants NAS of Ukraine, 03028 Kyiv, Ukraine
********Institute for Energy Security and Environmental Safety, Centre for Energy Research, Konkoly-Thege str. 29-33, 1121 Budapest, Hungary
(*Received 11 May 2020 • Revised 16 August 2020 • Accepted 6 September 2020*)

Abstract−Iron oxide-silica nanocomposites were prepared by sol-gel method using ammonia (NH_3), acetic acid (CH_3COOH) and hydrochloric acid (HCl) catalysts to generate different pH values for the reaction conditions. As starting precursors, for the silica, respectively, for the iron oxide, tetraethylorthosilicate (TEOS) and iron-III-acetylacetonate were used. The physico-chemical characterization of the materials revealed that the sample obtained with HCl catalyst displays the largest surface area (300 m^2/g), the most compact network structure, highest surface roughness, biggest crystallite size (14 nm), magnetization (7 emu/g) and superparamagnetic behavior. These materials were tested for adsorption of Cr^{6+} and Zn^{2+} from aqueous solution. Sample M-HCl presented the highest surface area and was further used for adsorption of metal ions. Kinetic, thermodynamic and equilibrium adsorption measurements studies were made for Cr^{6+} and Zn^{2+}. To establish the material behavior from a thermodynamic point of view, temperature and contact time of adsorption process, activation energy, free energy, of standard enthalpy and entropy were calculated. The kinetic behavior was modelled by pseudo-first-order, pseudo-second-order and intraparticle diffusion kinetic models and the adsorption characteristics were determined by modelling the experimental data with Langmuir, Freundlich and Sips isotherms.

Keywords: Magnetic Materials, Surfaces, Nanocomposites, Adsorption, Catalyst

INTRODUCTION

Water source pollution with heavy metals is one of the priority problems for the environment, representing a high hazard for human health. Cadmium, copper, chromium, lead, zinc, mercury and others are just some of few heavy metals with toxic proprieties that can harm human and animal organs by pollution of the water [1]. From these elements, Cr^{6+} is one of the most toxic elements, presenting different mutagen activity onto living organisms even in small quantity [2]. Even so, Cr^{6+} is still being used in galvanic coatings, textile and leather industries, fungicide production and for dyes and pigments [3,4]. On the other hand, Zn^{2+} can be found in wastewater obtained from the galvanic coatings industry, the processing industry, metallurgy, and also mining. Zinc ions present in water can affect the water environment due to oxidative processes [5]. Generation of wastewater containing chromium and zinc metal ions has led to the development of various techniques such as ion exchange, precipitation, reverse osmosis, and membrane separation, to recover these metal ions or minimize their negative impact on the environment [6,7]. The majority of these processes present some disadvantages such as high energy, large amounts of constituent and sludge waste [8]. Therefore, the development of new technology for wastewater treatment is of current interest. The technologies based on adsorption could be the next option with small costs for application and processing, making them more interesting. Many studies are dedicated to the development of new materials with adsorptive properties presenting a high durability and selectivity in order to remove a wide range of pollutants [9]. Due

†To whom correspondence should be addressed.
E-mail: adina.negrea@chim.upt.ro, putzanamaria@yahoo.com

to their high adsorption affinity and capacity [10] and the ease of separation, iron oxide-containing materials are of primary interest in this field. The use of bare iron oxides for wastewater treatment is limited due to the magnetically induced aggregation [11,12]. This problem could be overcome by covering the iron oxide with silica or other polymers, which also protects and allows better control of the morpho-textural, structural and magnetic properties [13-17]. Bashir et al. studied the effect of different pH solutions onto structural and magnetic properties of iron oxide nanoparticles [18]. In the same line, we report herein the preparation and the influence of the catalyst, alongside the pH, on the morpho-textural, structural, and magnetic properties of iron oxide-silica nanocomposites, for their subsequent use as heavy metal sorbents. We prepared three materials using one pot synthesis scheme by thermal decomposition of iron-III-acetyl acetonate and in situ coating with silica using TEOS precursor, and different catalysts, NH_3, CH_3COOH and HCl, and analyzed their structural and magnetic properties and adsorption performance of Cr^{6+} and Zn^{2+} ions from aqueous solutions.

MATERIALS AND METHODS

1. Materials Synthesis

Three silica-iron oxide materials (M-HCl, M-CH_3COOH, M-NH_3) were prepared using sol-gel method. Iron-III-acetylacetonate (Sigma-Aldrich), TEOS (Sigma-Aldrich), NH_3, CH_3COOH and HCl (Sigma-Aldrich), MeOH (Sigma-Aldrich) were used as received. A solution of 8 g of iron-III-acetylacetonate in 50 mL MeOH was magnetically stirred at 55 °C for 15 minutes and was poured over a solution of 15 mL TEOS in 15 mL distilled water. For each sample, 0.05 mL of catalyst--NH_3 (pH=10), CH_3COOH (pH=5) or HCl (pH=2)--was added and stirred for another 30 minutes and then ultrasonicated. A VCX-T-750 apparatus operating at 20 kHz and 750 W, with titanium sonotrode (1 cm diameter) was immersed (1 cm deep) into the sol. The sonotrode worked at 40% amplitude, with pulse sequence on/off - 5/5 sec. A 150 mL sample glass container was filled with 90 mL of liquid, containing the total volume of reactants, for each preparation. During sonication the temperature increased from 25 °C to 55 °C. The total transferred energy, including thermal dissipation, was 55 J/mL, for each sample. The resulting sols were first dried at 80 °C and subsequently thermally treated at 200 °C.

2. Materials Characterization

The XRD structure analysis was completed using an Ultima IV (RIGAKU) apparatus. The FT-IR spectra were recorded on KBr pellets using JASCO FT/IR-4200 apparatus. Raman spectra were obtained at room temperature with the MultiView-2000 SPM system (Nanonics Imaging Ltd.), equipped with a Shamrock 500i Spectrograph (ANDOR), using a laser with wavelength of 514.5 nm as the excitation source and 30 s exposure time. Quantachrome Nova 1200e apparatus was used to determine the surface area and porosity. The NovaWin software was used to evaluate the isotherms obtained. Imaging and roughness data were obtained with LEXT-3D measuring laser microscope OLS4000 with 405 nm laser light source. The magnetization measurements were performed with a manually manufactured hysteresis graph with 7k Oe magnetic field [19]. The small-angle scattering measurements were performed on the YuMO small-angle spectrometer [20] operating at the IBR-2 pulsed reactor in Dubna [21]. The scattered neutrons were detected using the time of flight method by a two-detector setup with ring wire detectors [22]. Measurements were performed on dry powders at room temperature. A vanadium standard was used for the calibration of absolute scattered intensity, while silver behenate sample was used to calibrate distances [23]. The measured scattering curves were corrected for transmission and the background scattering from an empty aluminium sample container using the SAS software [24]. To determine the point of zero charge (pzc), 0.1 g of M-HCl material was mixed with 25 mL of KCl 0.1 M solution. pH of the KCl solutions was adjusted in the range of 1-12 using NaOH solutions, with concentrations between 0.05-2 N or HNO_3 solutions, with concentrations between 0.05-2 N. After adjusting the pH, the samples were stirred for 1 hour at 200 rpm at 298 K, using a shaker bath with a Julabo SW23 thermostat. The samples were filtered and the pH of the resulting solutions was determined in the filtrate by using a pH meter of the Mettler Toledo, Seven Compact type.

3. Sorption Studies

The contact time and temperature are some of the few important factors for evaluation of affinity of the materials for Cr^{6+} and Zn^{2+} ions. To determine the influence of contact time and temperature on the adsorption capacity of the synthesized M-HCl material, 0.1 g material was weighed and added to 25 mL of Cr^{6+} and Zn^{2+} solutions of concentrations of 50 mg/L. The samples were stirred at 200 rot/min for 15, 30, 60, 120, 180 and 240 minutes in a mechanical shaker bath (JULABO SW23), thermostatted at different temperatures (298 K, 308 K and 318 K). Adsorption studies were performed at pH=4. To study the effect of the sorbent dose, different amounts of solid material (0.05; 0.1; 0.2; 0.3; 0.4; 0.5 g) were added to 25 mL metallic ion solution with concentration 50 mg/L. The samples were kept in contact for 60 minutes in a thermostatted shaker bath at 298 K, and 200 rpm. Next, the samples were filtered and the residual concentration of metal ions was determined in the filtrate by atomic absorption spectrometry. To study the effect of pH on the adsorption process of metal ions, 0.1 g of M-HCl material was accurately weighed and 25 mL of different solutions was added, with pH in the range of 1-8, for Zn^{2+} and pH in the range 1-6, for Cr^{6+}, at an initial concentration of metal ions of C_0=50 mg/L. Since at pH=8.5 for Zn^{2+} and pH=6 for Cr^{6+} begins the process of precipitation of hydroxides of the two metals, the adsorption was studied up to these pH values. The pH values were adjusted using 0.05-2 N, of NaOH and 0.05-2 N of HNO_3 solutions. The samples were stirred for one hour at 298 K in a shaker bath, then filtered and the residual concentration of metal ions in the filtrate was determined by atomic absorption spectrometry.

Equilibrium adsorption studies were conducted using 0.1 g adsorbent material and 25 mL metal ions solutions varying the initial concentration between 5 and 200 mg Cr^{6+}/L solution and between 5 and 100 mg Zn^{2+}/L solution. In this case, the contact time was 3 hours at 298 K, using a mechanical shaker bath at 200 rpm. All samples were then filtered and the residual concentration of Cr^{6+} and Zn^{2+} ions from the filtered solution was determined using a Varian SpectrAA 280 FS atomic absorption spectrometer.

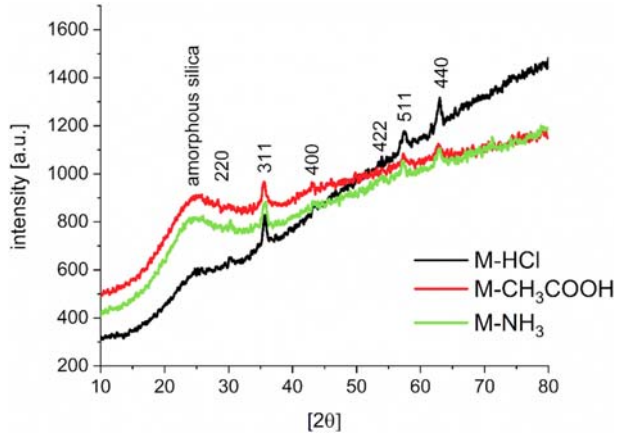

Fig. 1. X-ray diffractograms for samples prepared with different catalysts.

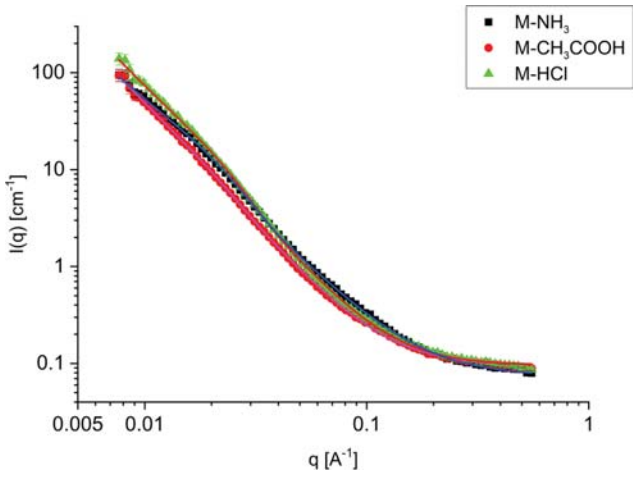

Fig. 2. SANS scattering curves of the nanocomposites. Symbols - experimental data, solid lines - model fits.

RESULTS AND DISCUSSION

1. XRD

The X-ray diffraction patterns are presented in Fig. 1 for the three samples prepared with different catalysts at three distinct pH.

All samples presented crystallinity, with peaks specific to cubic phase of iron oxide nanoparticles. Also, a broad maximum centered at 25° specific for amorphous silica was found in all samples. Three strong diffraction lines at 2θ angles of 37° (311), 57° (511) and 63° (440) were used to determine the mean crystallite size using the Scherrer equation [25]. The highest crystallite size with a value of 11 nm was obtained for M-HCl sample. For M-CH_3COOH and M-NH_3 samples the crystallite size was 7 nm and 9 nm, respectively.

2. Small-angle Neutron Scattering

The scattering intensity data, presented in Fig. 2, show a monotonic decaying intensity with increasing angle, characteristic for porous materials such as xerogels and composites with self-similar structure over different sizes from a few to 500 nm [26-28]. In double logarithmic representation, the deviations of the data from a straight line indicate the presence of structural features of a characteristic size, which can be in our case the magnetite nanoparticles embedded in the fractal-like xerogel networks. The data were modelled by Eq. (1).

Table 1. The structural parameters calculated from SANS

Sample	Rg, nm	P	χ^2
M-CH_3COOH	10.71±0.05	2.47±0.02	2.41
M-HCl	9.69±0.03	2.53±0.02	4.84
M-NH_3	9.76±0.03	2.24±0.02	4.76

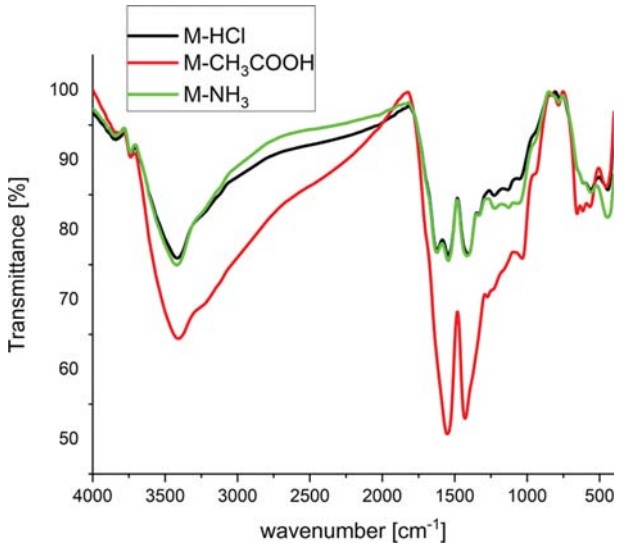

Fig. 3. FT-IR spectra for magnetic nanocomposites prepared with different catalyst.

$$I(q) = Aq^{-p} + B\exp(-q^2R_g^2/3) + bg \quad (1)$$

The first term describes a general power law scattering arising from self-similar structure of the porous xerogels, and the second term is a Guinier-term describing the iron oxide particles and their agglomerates. The third term is a free parameter representing an adjustable flat background. Fitting was performed by a home-made Monte Carlo least square minimization software. The structural parameters are collected in Table 1.

3. FT-IR and Raman Vibrational Data

The FT-IR spectra (Fig. 3) show the characteristic bands of $Fe(acac)_3$ at ~1,624 and ~1,541 cm^{-1} for M-HCl and M-NH_3 samples, respectively; they are weak due to the partial decomposition at 200 °C [29].

In case of M-CH_3COOH sample, the band presents only one intense peak at 1,550 cm^{-1} showing the complexation reaction with $Fe(acac)_3$ residue. The silica precursor bands were observed at ~1,050, ~800 and ~445 cm^{-1} for all samples. The band at 936 cm^{-1} for M-CH_3COOH sample indicates the Si-OH bonds. The peaks specific for maghemite appear at ~655, 615 and 560 cm^{-1} [30].

The two main Raman peaks around 500 cm^{-1} and 1,600 cm^{-1} in Fig. 4 are attributed to the ν(Fe-O) and ν(C-O) bonds, the last one being referred also as a coupled vibration between ν(C-C) and ν(C-O) [31,32]. Around the same values (500 cm^{-1} and 1,600 cm^{-1}) are expected to be found the Si-O bending and stretching bands

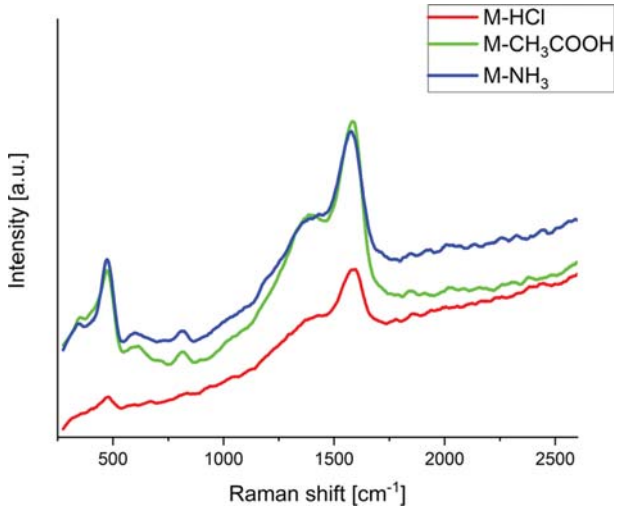

Fig. 4. Raman spectra for magnetic nanocomposites prepared with different catalyst.

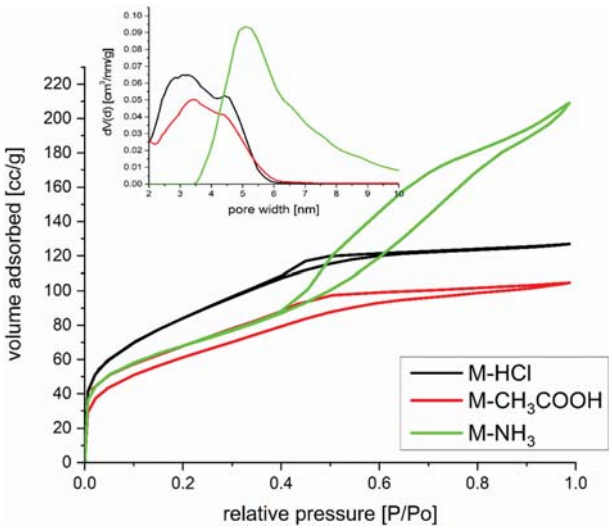

Fig. 5. N_2 adsorption-desorption isotherms for the samples prepared with different catalysts.

[33]. The changes in this region are mainly due to the Si substitutions with other metal ions that influence the connectivity to the terminal oxygen atoms, leading to changes in the Raman spectra [33]. Minor variations in band positions were observed between the M-HCl, M-NH_3 and M-CH_3COOH samples. Values of 473 cm^{-1} in case of M-NH_3 and M-CH_3COOH, respectively, 476 cm^{-1} in case of M-HCl, were detected, whereas for the second specific band, 1,576 cm^{-1} (M-NH_3), 1,585 cm^{-1} (M-CH_3COOH) and 1,588 cm^{-1} (M-HCl) were observed [31,32]. The shoulder at 1,370 cm^{-1} observed both in Raman and IR spectra corresponds to the combination of ν(C-O) and ν(C=C) stretches and $\delta(CH_3)$ bending [34]. The ~473-476 cm^{-1} band is also present due to the less significant contributions of bending vibration from CH-C-CH_3 as a result of Fe atoms shifting in the direction of the acetylacetonate's oxygen group [35]. The peak at 592 cm^{-1} corresponds to the O=C-CH_3 bending and is also is influenced by the CH-C-CH_3 bending and O-Fe stretching [35]. While a vibration is considered to be Raman active if it causes a change in polarizability, in case of the IR, the vibration mode is active only when there is a change in dipole moment. Therefore, a difference in the band intensity is visible when comparing the IR and Raman spectra, changes that may influence the Raman spectra are hydrogen bonding and modifications in the chain conformation which result in different electronic structure of the molecular unit [34]. Other influencing factors are crystal field splitting, chain packing and solvation interaction with the molecular unit which are contributing to the electronic structure of the molecular unit [34]. All aforementioned changes lead to shifts in the normal mode frequencies and line shapes [34]. The difference between the samples is also visible in the band intensity decrease, which shows an inverse behavior compared to the trend in magnetization. Slight amorphicity of the compound is more pronounced in the case of M-HCl, highlighted by the band shape [34]. Lower intensity and less defined bands are obtained, as expected, for the most acidic compound M-HCl [35]. The change in intensity of Raman peaks can be related to the pH, which affects the material's surface and influences the molecule reorientation and bonds on the terminal area [36,37]. We observed a positive correlation between pH and intensity; thus, by increasing pH value the peak intensity also increases. It was observed that at lower pH value, peak alteration may occur [37].

4. N_2 Adsorption-desorption Isotherms

Prior to the analysis, the samples were degassed in vacuum for 4 hours at 100 °C. In Fig. 5 the N_2 adsorption-desorption isotherms with the pore size distribution are shown.

Sample M-NH_3 exhibits a type IVa isotherm according to IUPAC classification [38], indicating mesoporous material with hysteresis of type H2b, with plate-like pores. Isotherms for samples M-HCl and M-CH_3COOH are of type H4, indicating conical shaped pores and micro porosity. The textural data are collected in Table 2.

For efficient adsorption of heavy metal pollutants, a high surface area is mandatory [39]. The surface area was evaluated by Brunauer-Emmett-Teller (BET) method. Sample M-HCl presented the highest surface area with the value of 300 m^2/g and total pore volume

Table 2. Textural parameters calculated from N_2 adsorption isotherms

Sample name	BET surface area, m^2/g	Pore width, nm	Total pore volume, cc/g	FHH, Fractal dimension
M-HCl	300	3	0.197	2.8598
M-CH_3COOH	219	3.4	0.219	2.8415
M-NH_3	241	5	0.324	2.6687

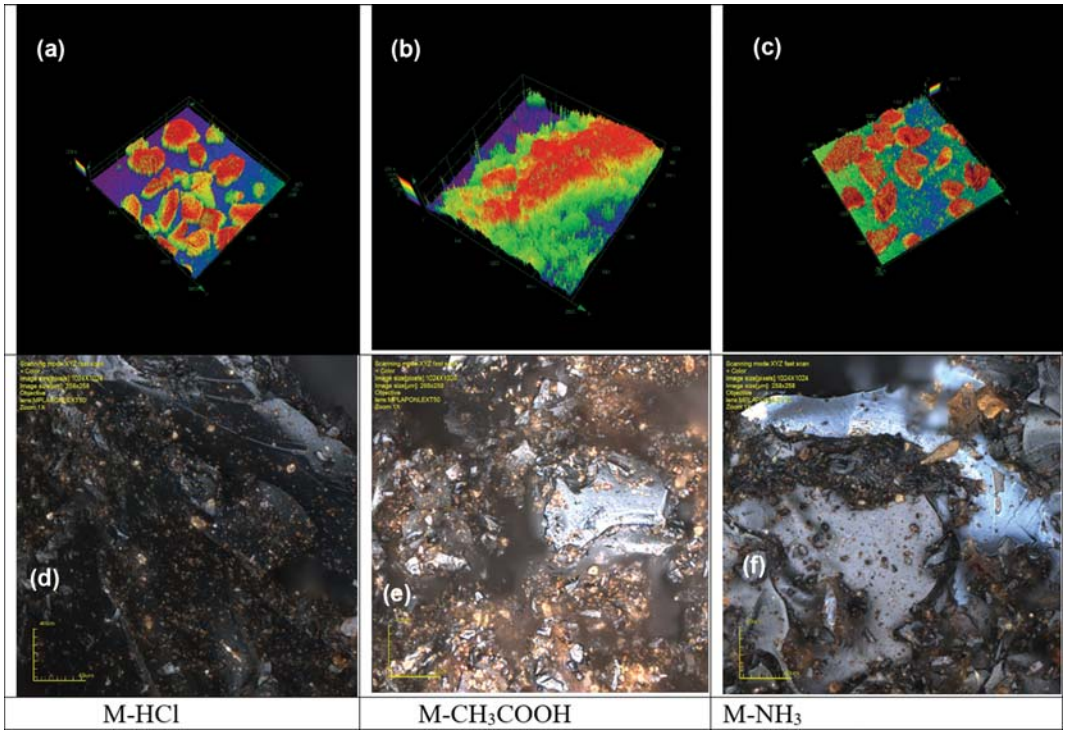

Fig. 6. 3D laser microscopy images for sample with different catalyst.

of 0.197 cm^3/g, while M-NH_3 and M-CH_3COOH had lower values: 241 m^2/g with a total pore volume of 0.324 cm^3/g, and 219 m^2/g with a total pore volume of 0.162 cm^3/g, respectively. Further, the pore size distribution was evaluated using the non-linear density functional theory (NL-DFT) equilibrium model. A general trend can be observed that the porosity is decreasing when the pH of catalyst is lower (Table 2). From Frenkel-Halsey-Hill (FHH) adsorption-activation method, the highest value of rugosity was obtained for M-HCl. To calculate the degree of micro porosity, the external and micropore surface was considered from the V-t method in the 0.15-0.55 P/P_0 domain. In case of M-HCl we obtained a 50% micro porosity, 25% micro porosity for M-CH_3COOH and no micro porosity for M-NH_3. It was observed that basic conditions in the sol-gel synthesis lead to an increase in the material's mesoporosity, which also confirms the influence of the pH of catalyst solution on the morphology of the obtained materials.

Table 3. Calculated values from 3D laser microscopy images

Sample	Average roughness (Sa)	Mean square root roughness (Sq)	Maximum peak height (Sp)	Maximum valley depth (Sv)	Maximum peak-to valley height (Sz)	Surface kurtosis (Sku)	Surface skewness (Ssk)
M-CH_3COOH	258 μm×258 μm						
	20.35	30.7	132.9	144.99	277.85	7.46	−0.59
	40 μm×40 μm						
	1.20	1.6	5.2	16.19	21.36	4.36	−0.38
M-HCl	258 μm×258 μm						
	4.90	9.7	92.4	136.29	228.69	30.87	1.09
	40 μm×40 μm						
	1.85	4.5	8.0	77.05	85.07	105.33	−8.71
M-NH_3	258 μm×258 μm						
	4.07	5.6	33.9	18.68	52.66	5.37	0.79
	40 μm×40 μm						
	0.37	0.6	5.1	0.62	5.73	18.19	3.25

5. 3D Laser Microscopy Images and Roughness Data

From the 3D laser microscopy images of the three samples (Fig. 6), the calculated values of average roughness (Sa), mean square root roughness (Sq), maximum peak height (Sp), maximum valley depth (Sv), maximum peak-to valley height (Sz), surface kurtosis (Sku) and surface skewness (Ssk) are obtained and shown in Table 3:

All analyzed samples were investigated on a 40 μm×40 μm area and on the entire area (258 μm×258 μm). For every specified sample and area, ten measurements were performed to eliminate possible measurement errors. In the 258 μm×258 μm analysis, the highest roughness in both Ra and Rq values was obtained for the M-CH_3COOH sample, followed in decreasing order by the M-HCl and M-NH_3 samples. In case of 40 μm×40 μm roughness analysis, highest roughness was found for the M-HCl, followed by M-CH_3COOH and M-NH_3. Note that the 40×40 area was selected on flatter surfaces in all three cases. Higher roughness in case of M-CH_3COOH (258 μm×258 μm) and M-HCl (40 μm×40 μm) is the result of a higher Sz value, which is obtained from the sum of Sp and Sv values. This result indicates the presence of higher peaks and lower valleys in comparison to other materials. According to the asperity results (Ssk) for M-HCl (40 μm×40 μm), and M-CH_3COOH samples negative values were obtained, indicating porous surfaces and majority of pits. Sku indicated the presence of peak or valley defects, which in this case are present on the surface of all analyzed samples. The rugosity data from 40×40 μm area corresponds with the textural parameters data from N_2 adsorption-desorption isotherms, indicating the highest rugosity of M-HCl sample and the lowest rugosity in the case of M-NH_3, which also can be correlated with the pore shape, in the last case, plate shape indicating lower peak to valley height (Sz) for M-NH_3, whereas the higher rugosity (M-HCl and M-CH_3COOH) have similar pore shape. In the case of 258×258 μm area, there is a slight difference which occurs due to the larger examination area, with the higher risk of intercalation of crystals, resulting in different rugosity values.

6. Magnetization

In Fig. 7 the magnetization curves are plotted. M-HCl presents the best magnetization saturation having a value of 7 emu/g with a coercive field of 0.03 kOe. For M-NH_3 the magnetization saturation value is 5 emu/g with a coercive field of 0.009 kOe, followed by M-CH_3COOH with a magnetization value of 4 emu/g and a coercive field of 0.02 kOe. The magnetization data indicate superparamagnetic behavior for all samples.

7. Sorption Studies

7-1. Point of Zero Charge (pHpzc)

The point of zero charge (pHpzc) is generally described as the pH at which the net charge of the total surface area of the particles (i.e., the surface of the absorbent) is zero, a concept that has been introduced in studies concerning the colloidal flocculation in order to explain the pH affecting this phenomenon [40]. From the experimental data plot, Fig. 8, it is observed that the M-HCl material has pHpzc=4; thus, the range in which it is recommended to perform adsorption is the pH interval, 2-6.

7-2. Effect of the Adsorbent Material Dose

The efficiency of the adsorption process is calculated according to Eq. (2):

$$\eta = \frac{Ci - Crez}{Ci} \cdot 100 \quad (2)$$

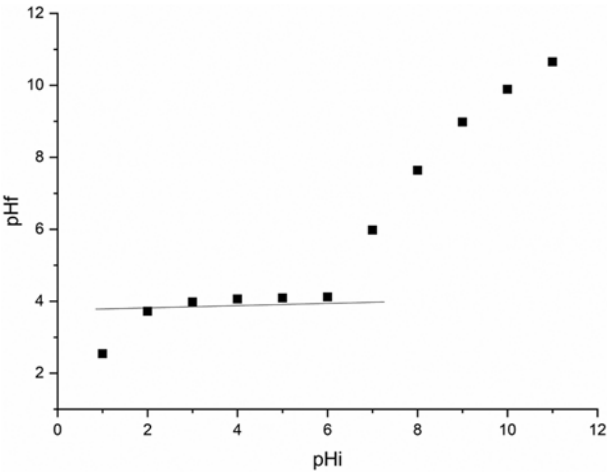

Fig. 8. pHpzc for M-HCl material.

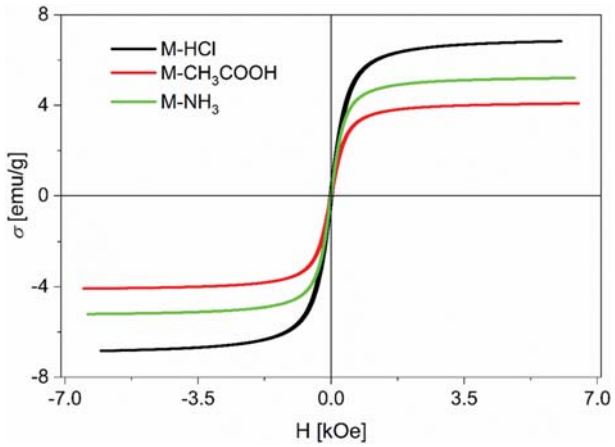

Fig. 7. Magnetization curves for the samples synthetized with different catalysts.

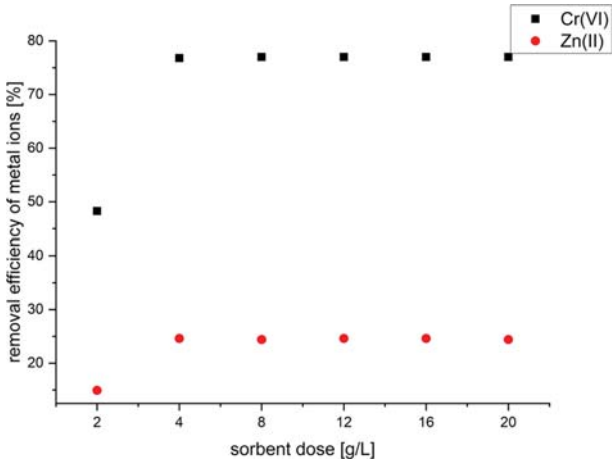

Fig. 9. Effect of the adsorbent material dose on Cr^{6+} and Zn^{2+} adsorption process from aqueous solutions.

where Ci is the initial concentration of metal ion in the solution and Crez is the residual concentration of metal ion in the solution following the adsorption process. The influence of dose of adsorbent material on Cr^{6+} and Zn^{2+} adsorption process is shown in Fig. 9. It is found that the dose of adsorbent material influences the removal efficiency of Cr^{6+} and Zn^{2+}. Thus, in the case of Cr^{6+} adsorption the removal efficiency is ~80%, starting with a dose of 0.1 g of material in 25 mL of initial solution with Cr^{6+} concentration of 50 mg/L. In the case of Zn^{2+} adsorption, the removal efficiency is ~25%, starting with 0.1 g of solid material in 25 of initial solution with Zn^{2+} concentration of 50 mg/L. Higher sorbent material concentrations in these conditions are therefore unnecessary.

7-3. Effect of pH on Adsorption

The pH of the aqueous solution is a crucial parameter for the process of removal of metal ions by adsorption [41]. The pH of Cr^{6+} was studied in the range of 1-6, and the pH of Zn^{2+} in the range of 1-8. No studies have been performed at higher pH values because the two ions precipitate. From the data presented in the Fig. 10, with the increase of pH to pH=4 the adsorption capacity of the two ions increases to pH 4, and then remains constant, reaching q~9 mg/g for Cr^{6+} and q~3 mg/g for Zn^{2+}.

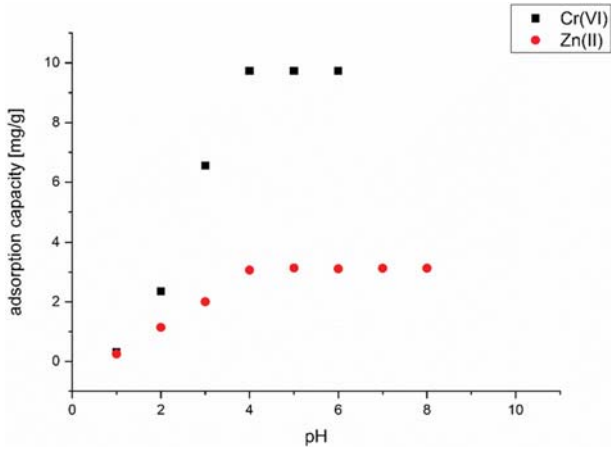

Fig. 10. pH effect on the adsorption process of Cr^{6+} and Zn^{2+} from aqueous solutions using M-HCl material.

7-4. Kinetic Studies

7-4-1. Pseudo-first-order and Pseudo-second-order Kinetic Models

Kinetic studies of adsorption process for Cr^{6+} and Zn^{2+} on sam-

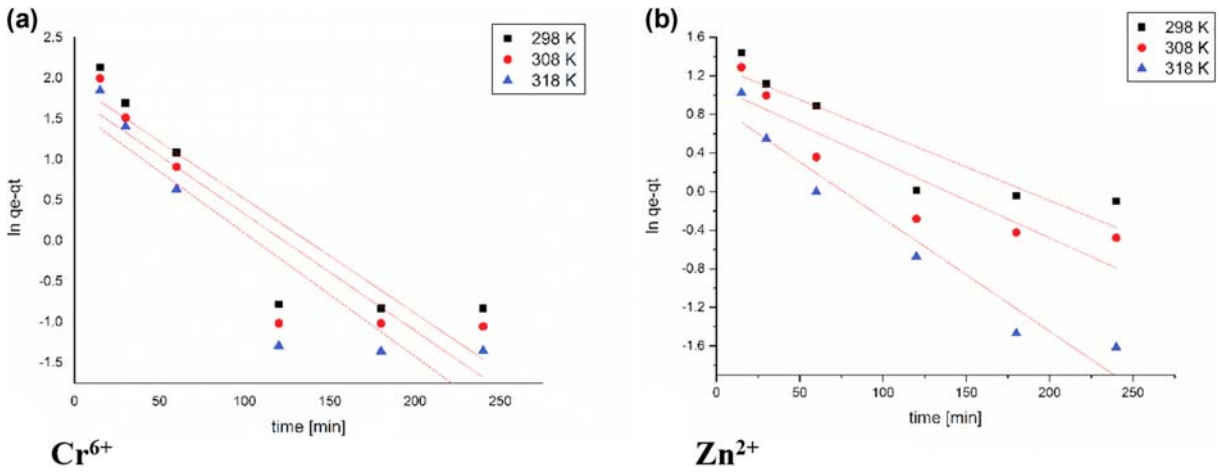

Fig. 11. Pseudo-first-order kinetic model.

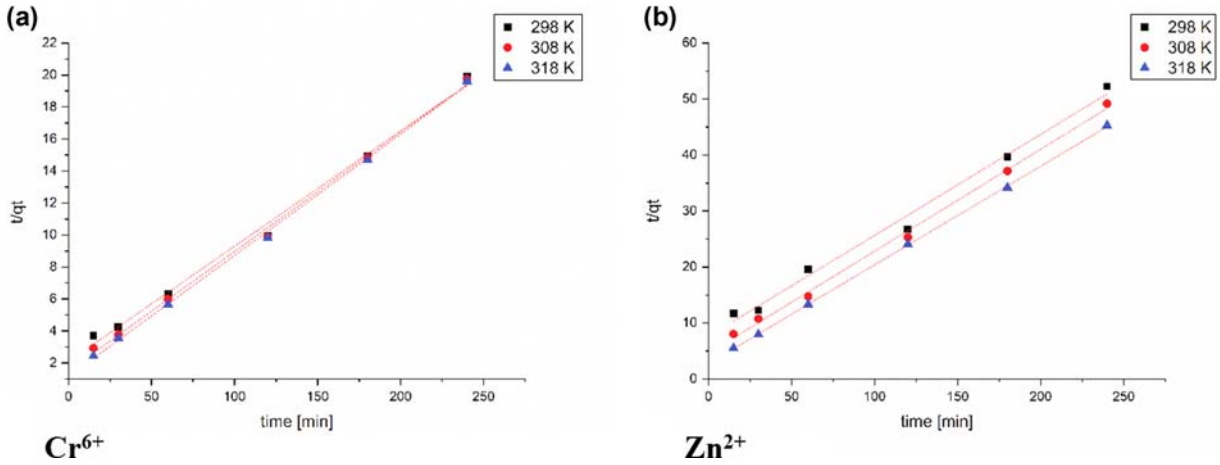

Fig. 12. Pseudo-second-order kinetic model.

Table 4. Kinetic parameters for adsorption of Cr^{6+} and Zn^{2+} ions adsorption onto M-HCl material

	Pseudo-first-order kinetic model					Pseudo-second-order kinetic model			
T, K	$q_{e,exp}$, mg/g	$q_{e,calc}$, mg/g	k_1, min^{-1}	R^2	χ^2	$q_{e,calc}$, mg/g	k_2, min^{-1} $(mg/g)^{-1}$	R^2	χ^2
					Cr^{6+}				
298	12.04	6.87	0.0141	0.8244	0.55	12.06	69.71	0.9943	0.082
308	12.14	5.85	0.0144	0.214	0.45	12.21	98.72	0.9999	0.081
318	12.23	5.25	0.0151	0.8235	0.44	14.08	124.4	0.9975	0.071
					Zn^{2+}				
298	4.49	3.67	0.007	0.8484	0.21	5.54	4.033	0.9909	0.027
308	4.75	2.95	0.0078	0.8348	0.28	5.48	6.55	0.9972	0.031
318	4.99	2.35	0.0118	0.9458	0.23	5.67	12.02	0.9998	0.033

ple M-HCl were conducted by modelling the experimental data using pseudo-first-order (Fig. 11(a) and 11(b)) and pseudo-second-order (Fig. 12(a) and 12(b)) kinetic models. Kinetic parameters for both models are presented in Table 4.

For both metal ions, Cr^{6+} and Zn^{2+}, the value of the regression coefficient, in the case of the pseudo-first-order kinetic model is smaller than in the case of the pseudo-second-order kinetic model, showing that the pseudo-second-order kinetic model better describes the adsorption process of the metal ions on the M-HCl material. These results agree with literature data according to which the adsorption process depends on the temperature and at the same time the chemical reactions can represent the limiting factor for adsorption process kinetics. Also, due to the relatively short time required to saturate the contact surface of the material, it can be considered that the adsorption process takes place without mass transfer in solution [42,43]. It can be assumed that over time the adsorption of metal ions in the solution takes place, the formation of strong chemical bonds established by attraction forces and ion exchange between them and the substrate. Using the value of the kinetic constant k_2 obtained and the Arrhenius equation, the value of the activation energy, Ea, can be determined and associated with the adsorption process. Thus, the activation energy is calculated from the linearized graph representing $\ln k_2$ as a function of 1/T (Fig. 13).

The activation energy Ea in the case of Cr^{6+} adsorption (22.8 kJ/mol) is less than 40 kJ/mol, corresponding to physical adsorption, while in the case of Zn^{2+} adsorption, the activation energy Ea (53.1 kJ/mol) is bigger than 40 kJ/mol, which allows us to state that the adsorption process is physico-chemical adsorption [44].

7-4-2. Intraparticle Diffusion Kinetic Model

The mechanism of adsorption can be discussed from different points of view. One is the intraparticle diffusion kinetic model, which gives information about the limits of batch adsorption. Thus, if the pseudo-first-order and pseudo-second-order kinetic models cannot provide very clear information about the adsorption mechanism, intraparticle diffusion can provide this information more accurately. The adsorbate is assumed to be initially transferred on to the surface which is then transported to the available sites by a diffusion process in this model and the formation on a boundary layer is finally followed by the interaction of adsorbent within the sites [45]. For the present study, the first 10 minutes can be attributed to the mass transfer that takes place by diffusion through the boundary layer, while the final linear part indicates intraparticle diffusion, which refers to the highest diffusion in the pores of the material

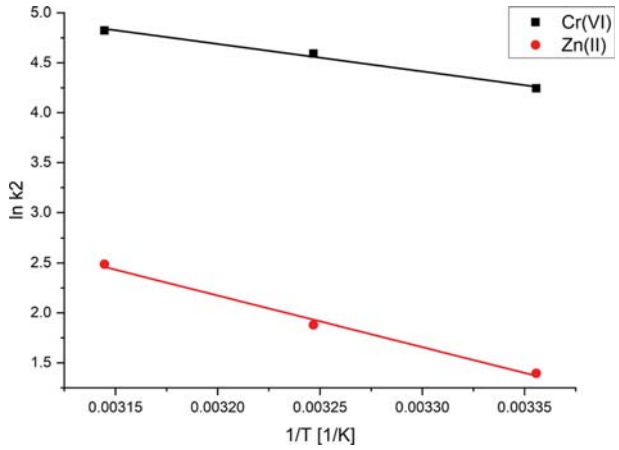

Fig. 13. $\ln K_2$ versus 1/T for Cr^{6+} and Zn^{2+} ions adsorptions onto M-HCl material.

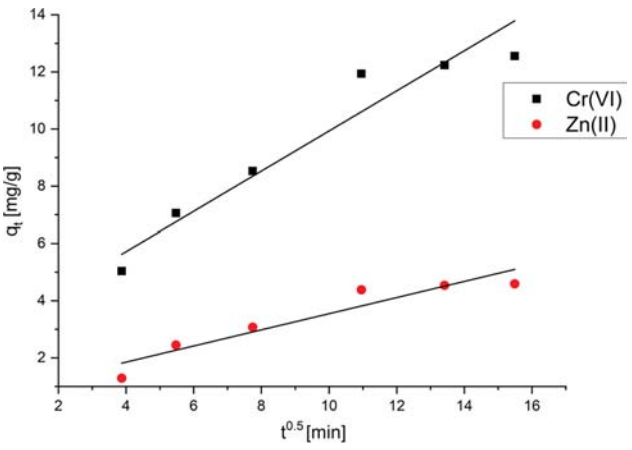

Fig. 14. Intraparticle diffusion for adsorption of metal ions onto the M-HCl material.

Table 5. The intraparticle diffusion model parameters for the adsorption of metal ions onto M-HCl material (work conditions: initial concentration of Cr^{6+} and Zn^{2+} 50 mg/L, temperature 298 K, pH=4, agitation rate 120 rpm)

Metal ion	Intraparticle diffusion model		
	K_{diff} (mg·g^{-1} min$^{-1/2}$)	C	R^2
Cr^{6+}	2.91	0.70	0.8388
Zn^{2+}	0.72	0.28	0.8609

[46,47]. To distinguish if film diffusion or intraparticle diffusion is the determining rate step, the kinetic experimental data were processed according to the Weber and Morris model, Eq. (3):

$$q_t = k_{diff} \bullet t_{1/2} + C \quad (3)$$

where q_t - adsorption capacity at time t; k_{diff} - kinetic constant of intra-particle diffusion (mg g^{-1} min$^{-1/2}$); and C - a constant correlated with the thickness of the liquid film around the adsorbent particles.

The intraparticle diffusion for adsorption of metal ions onto M-HCl material is represented in Fig. 14.

It is observed, in Table 5, from the value of the diffusion constant, Kdiff, that in the case of Cr^{6+} the diffusion in the pores of the material is higher than in the case of Zn^{2+}. In the case of Zn^{2+} it can be stated that the value of the diffusion constant is influenced by intraparticle diffusion resistance and in the micro and the mesopores of the material was higher. In the case of Cr^{6+} adsorption it can be concluded that the adsorption process proceeds faster [47]. The fact that the linearized curve does not pass through the origin demonstrates that the pore diffusion of metal ions during adsorption influences the kinetics of the adsorption process.

7-5. Thermodynamic Studies

The adsorption capacity of the M-HCl material depends on the contact time and temperature. Figs. 15(a) and 15(b) show the influence of contact time and temperature on the adsorption capacity of the M-HCl material.

To obtain information on the energy changes associated with the adsorption process, thermodynamic studies were carried out in the temperature range 298-318 K. Based on the data obtained from the thermodynamic studies, it could be concluded whether the adsorption process is spontaneous or not. Thus, the variations of standard enthalpy, ΔH^o, standard Gibbs free energy, ΔG^o, and standard entropy, ΔS^o, were determined. From the linear representation of the dependence of K_d as a function of 1/T (Fig. 13), the variation of standard entropy and the variation of the standard enthalpy were determined. Subsequently, the variation of Gibbs free energy was evaluated using the van't Hoff equation. The obtained thermodynamic parameters are presented in Table 6.

Table 6. Thermodynamic parameters for the adsorption of Cr^{6+} and Zn^{2+} ions adsorption onto M-HCl material

Metal ion	Temperature, K	ΔG^o, kJ/mol	ΔH^o, kJ/mol	ΔS^o, kJ/mol·K
Cr^{6+}	298	−4.72	19.54	81.46
	308	−5.54		
	318	−6.36		
Zn^{2+}	298	−1.98	6.73	89.17
	308	−2.07		
	318	−2.16		

Negative Gibbs free energy values suggest that adsorption of metal ions occurs spontaneously. Also, decreasing the value of Gibbs free energy with temperature increase shows that the adsorption process of metal ions is favored by increased temperature. The positive values of the standard enthalpy confirm that the adsorption process is endothermic, supported by the slight increase of the adsorption capacity at equilibrium and the kinetic constant (k_2) of pseudo-second-order as the temperature increases. The entropy change being positive suggests that the adsorption causes a greater disorder at the liquid-solid interface.

7-6. Equilibrium Studies

The Langmuir, Freundlich and Sips adsorption isotherms describing the adsorption process of the metal ions on the M-HCl material are shown in Fig. 16. The specific parameters of the studied

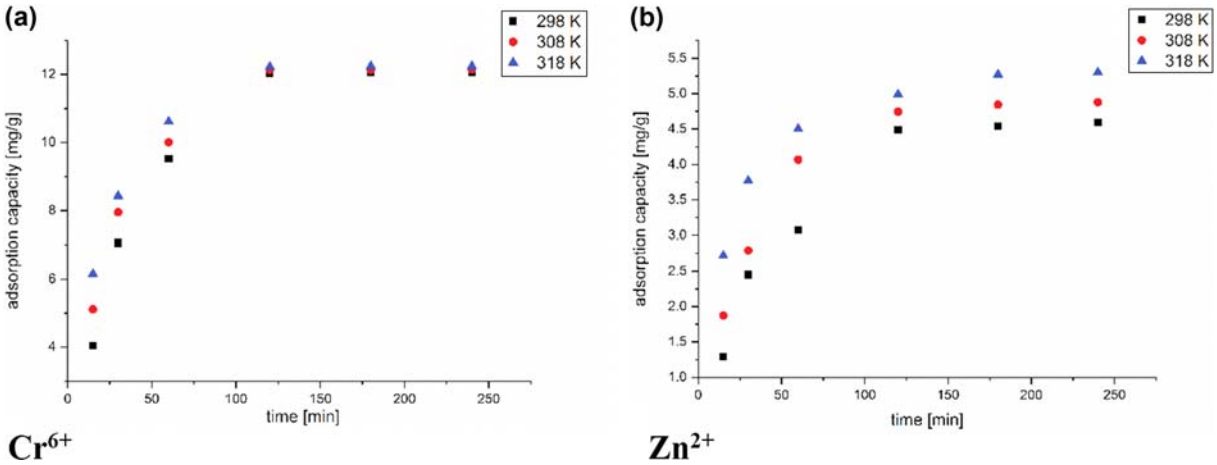

Fig. 15. Contact time and temperature effect on the adsorption process in the M-Cl material.

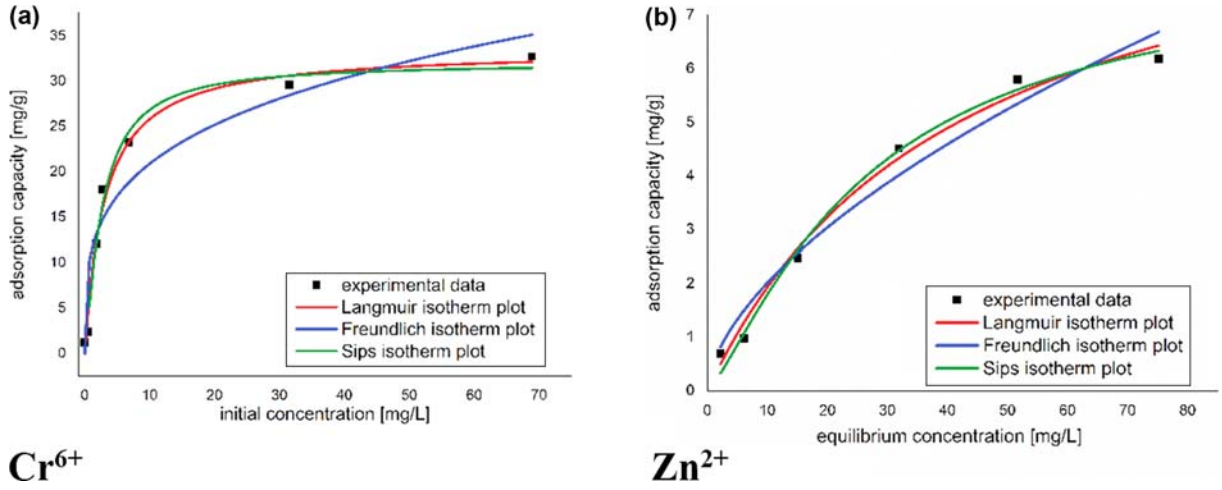

Fig. 16. Sorption isotherms models.

Table 7. Langmuir, Freundlich and Sips isotherm parameters for Cr^{6+} and Zn^{2+} ion adsorption onto M-HCl material

Metal ion	$q_{m,exp}$ mg/g	Langmuir			Freundlich			Sips			
		q_L, mg/g	K_L	R^2	K_F, mg/g	$1/n_F$	R^2	K_s	q_s, mg/g	$1/n_s$	R^2
Cr^{6+}	29.6	34.04	0.017	0.9929	11.2	0.27	0.8866	0.31	32.1	0.23	0.9989
Zn^{2+}	6.2	10.0	0.024	0.9861	0.51	0.59	0.9567	0.015	8.04	0.26	0.9873

isotherms are presented in Table 7.

From the data presented in Table 7 it can be seen that the adsorption process of the metal ions is modelled well by the Sips isotherm, based on the value of the regression coefficient [48]. This suggests that the adsorption mechanism is that of the monolayer adsorption.

CHARACTERIZATION OF THE MATERIALS AFTER THE ADSORPTION OF Cr^{6+} AND Zn^{2+}

1. FT-IR Spectroscopy Analysis after Adsorption

From the FT-IR spectra presented in Fig. 17 it is observed that in the band assigned to the hydroxyl groups, the peaks at 3,738 and 3,837 cm^{-1} of the starting material M-HCl, disappear after adsorption.

The vibrational specific bands of the Fe-O and Si-OH bonds are present at wave numbers 443, 559 and 778 cm^{-1} which, following the adsorption process, are shifted to higher wave numbers and decrease in magnitude. In case of sample M-HCl-Cr, sharp peaks appear in the 1,600-400 cm^{-1} interval, confirming the appearance of Cr-O bonds [49]. In the FT-IR spectrum for the adsorbent material after Zn^{2+} adsorption the sharp peak at ~3,417 cm^{-1} remains sharp but shifts to ~3,425 cm^{-1}, and the peak specific to the OH vibration from the wave number 3,837 cm^{-1} disappears while the peak at 3,738 cm^{-1} shifts to 3,775 cm^{-1}. The Zn-O bond is highlighted by the appearance of a vibration at wave number 465 cm^{-1} [50].

2. Raman Spectroscopy after Adsorption

After adsorption, chromate compounds are visible also in the Raman spectra, Fig. 18. The peak at 1,030 cm^{-1} resulted due to the

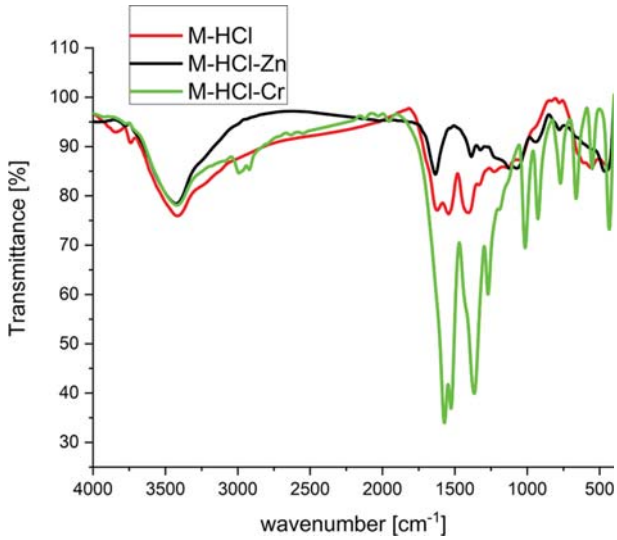

Fig. 17. FT-IR spectra after adsorption of the metallic ions on magnetic nanocomposite.

reaction between chromate ions in the solution and iron oxide nanoparticles [49]. According to the literature, the expected peak specific for the chromium compounds is between 800 and 1,030 cm^{-1} [49]. In our case the 1,030 cm^{-1} peak is very low in intensity due to the small amount of introduced Cr^{6+} in comparison to the iron III acetyl acetonate. This situation was also referred in another study [51] which explains the obscurity of the chromium peaks due to the co-existent ones ($Fe(acac)_3$ in this case), as well as the low signal and high noise levels in the measurements. The contri-

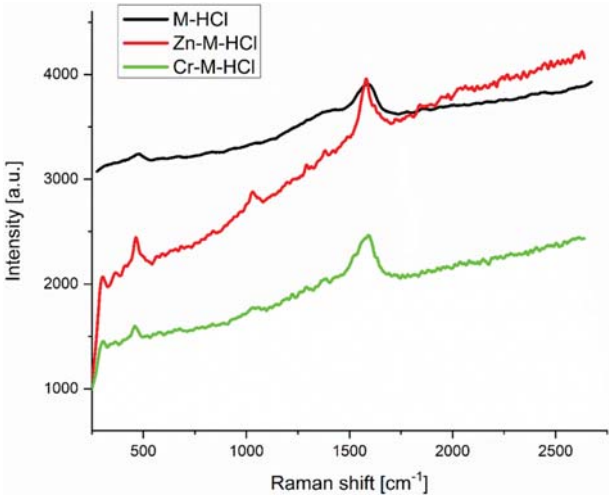

Fig. 18. Raman spectra for the magnetic nanocomposites prepared with HCl after adsorption of Cr^{6+} and Zn^{2+}.

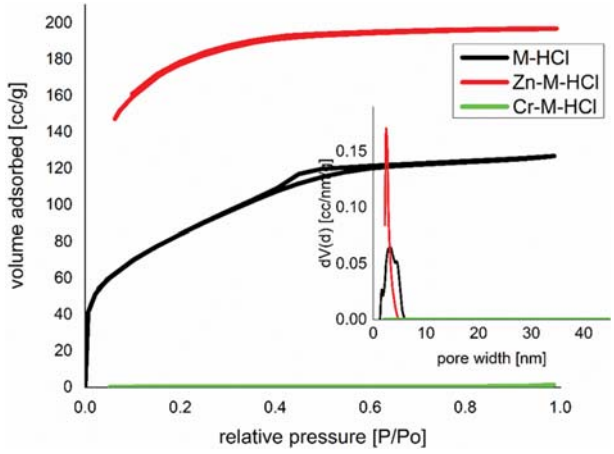

Fig. 19. Nitrogen adsorption isotherms and the pore size distribution of M-HCl nanocomposite before and after adsorption of metal ions.

bution of the Raman spectra is mainly to its possibility to detect the Cr^{6+} both from the surface and the bulk material, proving the adsorption ability of the present material [51]. In the case of Zn^{2+} absorption, the same peak around 1,030 cm^{-1} is present indicating the same type of bonding as in case of Cr^{6+}. While the Cr^{6+} solution resulted in higher metal adsorption, in the case of Zn^{2+}, the specific peak is seen to be more intense due to the better surface adsorption [51]. The ratio of the metal/acetylacetonate peaks differs for the two materials, being higher in the case of Zn^{2+} adsorption as a consequence of possible diffusion reaction and therefore better surface adsorption [51]. The obtained peaks indicate surface modifications, with the presumption that the ionic radius (Cr^{6+}=0.44 Å, Zn^{2+}=0.74 Å) [52], is the main reason for the Zn adhesion on the surface of the material. However, greater "infiltration" of the Cr^{6+} and better adsorption in the depths of the compound was obtained due to the smaller ionic radius confirmed by the sorption test [53]. The higher overall intensity of all peaks for the spectra with Zn^{2+} is also attributed to the fluorescence of the Zn containing materials [54]. The characteristic peak at 1,370 cm^{-1} in Raman spectra for the nanocomposites prepared with different catalysts becomes more distinguishable after Cr^{6+} and Zn^{2+} adsorption, resulting in two smaller peaks (~1,366-1,384 cm^{-1} and ~1,282-1,291 cm^{-1}). This may be due to the formation of $Fe(acac)_2(M)$ (M=Zn^{2+} or Cr^{6+}) type compounds in which case the C-O and C=C stretching frequencies are modified or shifted [55]. In $Fe(acac)_3$, there is a symmetrical chelate ring and two equivalent C-O and C=C bonds, therefore incorporating additional metals will result in shifts of these vibration bands to higher or lower frequencies [55].

3. N_2 Adsorption-desorption Isotherms after Adsorption of Cr^{6+} and Zn^{2+}

The isotherms obtained revealed for sample Zn-M-HCl a type Ib isotherm, specific for mesoporous material with a small quantity of micro porosity and in case of sample Cr-M-HCl a type II isotherm specific for non-porous material. In Table 8 the textural parameters are presented.

It can be seen that the adsorption of the two metal ions produces different changes of the surface area and pore volume. Thus, after the adsorption of Cr^{6+} the surface of the material decreases substantially from 300 m^2/g to 0.64 m^2/g, and the pore volume decreases from 0.197 cm^3/g to 0.002 cm^3/g. This can be explained by noting that Cr^{6+} ions in the form of chromate, dichromate enter and fill the pores of the material. On the other hand, in the case of Zn^{2+} adsorption, the surface area value doubles, reaching 645 m^2/g and the pore volume increases to 0.305 cm^3/g, which can be caused by forming Si-O-Zn bonds extending over the solid silica network. The OH groups covering the surfaces of the solid glassy network of SiO_2 allows the formation of Si-O-Zn bonds. This process can be seen by the disappearance of OH bands from the FT-IR spectrum and the appearance of Si-O-Zn bonds (Fig. 17).

4. Mechanism of Adsorption

The mechanism of the adsorption process of Cr^{6+} and Zn^{2+} on the M-HCl material goes as follows. The pH of the aqueous solution is a significant parameter for the removal of metal ions by adsorption [56]. The adsorption of Cr^{6+} in the pH range from 1-6 was studied and the experimental results reveal that with the increase of pH, the adsorption capacity increases up to ~9.7 mg/g at pH 4. Cr^{6+} exists in the aqueous phase in various anionic forms

Table 8. Textural parameters calculated from N_2 adsorption isotherms

Sample name	Langmuir surface area, m^2/g	BET surface area, m^2/g	Pore width, nm	Total pore volume, cm^3/g	FHH, Fractal dimension
M-HCl	329	300	3	0.197	2.859
M-HCl-Zn	870	645	2.4	0.305	2.889
M-HCl-Cr	0.93	0.64	3.3	0.002	1.739

Table 9. Adsorption capacities of some adsorbents cited in the literature

Adsorbent	Adsorption capacities, mg/g		Reference
	Cr^{6+}	Zn^{2+}	
Chitosan supramolecularly cross-linked with trimesic acid, CTMA	20	-	[58]
Rice straw	3.2	-	[59]
N,N-dimethylaminoethylmethacrylate-polypropylene	16	-	[60]
MnO_2	1	-	[61]
Carbon nanotubes, CNTs	-	0.17	[62]
Zirconium-aluminum pillared clays	0.715	0.572	[63]
Silica functionalized with mono amino and mercapto groups	12.36	-	[64]
Maghemite nanoparticles	6.53-10.17	-	[65]
Carboxylatedbiochar	18.2	-	[66]
Magnetic biochar	27.2	-	[66]
N-doped carbon with magnetic particles	16.0	-	[67]
γ-Fe_2O_3@cellulose aerogels	10.2	-	[68]
Fe_3O_4@n-SiO_2 nanoparticle	3.8	-	[69]
Maghemite	19.2	-	[70]
Mesoporous SiO_2-Fe_2O_3	7.2	-	[71]
Maghemite nanoparticles	2.62	-	[72]
Fe_2O_3/AlSBA-15	1.3	-	[73]
Fe_2O_3 - SiO_2 composite	6.17	-	[74]
Magnetic magnetite nanoparticle	8.67	-	[75]
Nanocelluloseferroferric oxide hybrid aerogel	2.2	-	[76]
magnetite nanoparticles	23	-	[77]
γ-Fe_2O_3		4.79	[78]
Fe_2O_3-ceramisite	-	7.4	[79]
γ-Fe_2O_3	-	19.23	[80]
Magnetic biochar (Fe_2O_3-EC)	-	9.42	[81]
Magnetic maghemite (γ-Fe_2O_3) nanotubes	-	84.95	[82]
M-HCl	29.6	6.2	This paper

such as chromate $[CrO_4]^{2-}$, dichromate $[Cr_2O_7]^{2-}$ or hydrogen chromate $[HCrO_4]^-$. The dominant form of Cr^{6+} at low pH is $[HCrO_4]^-$ [41]. From these results, it can be concluded that the chromium adsorption mechanism is achieved by the active form of Cr^{6+} which is adsorbed on the surface of the material by electrostatic bonding or by hydrogen bridges to it. Adsorption capacity is increasing with the pH, up to pH value of 4. At such low pH, the removal percentage of Cr^{6+} is high because the adsorption surface is protonated; thus, the strong electrostatic forces lead to attraction of Cr^{6+} anionic species to the adsorbent. The constant level of adsorption above pH=4 may be due to the saturation of the adsorption sites of anionic species, such as $[CrO_4]^{2-}$ and $[Cr_2O_7]^{2-}$, which delays the adsorption of Cr^{6+} ions on the surface of the M-HCl material. Thus, because the pH has risen above the zeta potential of the adsorbent, there is a reduction in the electrostatic attraction between the Cr^{6+} species and the adsorbent surface [41].

In the case of Zn^{2+} adsorption can be achieved by electrostatic attractions bonds [57] and forming Si-O-Zn groups on the silica surface. Adsorption of Zn^{2+} to the composite material remains unchanged above the pH=4. Adsorption of Zn^{2+} to the composite material decreases below pH=4 (Fig. 10). This could be due to the increase of the amount of H^+ in the adsorption centres.

According to the comparative data presented in Table 9, regarding other materials used for Cr^{6+} and Zn^{2+} adsorption from aqueous solutions, it is seen that our silica-iron oxide nanocomposites have a high adsorption capacity and can be used with good efficiency.

Due to their good removal efficiency and stability in aqueous solutions, these materials can be used as adsorbents for removal of Cr^{6+} and Zn^{2+} ions from wastewaters. It was also found that the studied material has higher affinity for Cr^{6+} ions, with adsorption capacity of ~30 mg/g, in comparison to the Zn^{2+} ions, that achieved adsorption capacity of ~6 mg/g.

We performed SEM measurements before and after adsorption and included them into the Supplementary Material.

DESORPTION STUDIES

Desorption studies help to elucidate the nature of the adsorption and to establish the recycling capacity of the depleted adsorbent and the recovery of the adsorbed metal ions from the solution [83,84]. For desorption 1 g of adsorbent material was taken, which was stirred for 4 h in contact with a 1 M solution HCl/HNO_3. After depletion, the sample was filtered and the amount of desorbed metal ions (Cr^{6+} or Zn^{2+}) in solution was determined. Desorption

amount of approximately 96% for Cr^{6+} and about 94% for Zn^{2+} was reached. From the solution, the metal ions can be concentrated, purified and then reused in various industrial processes, and the sorbent material can be reused in subsequent adsorption processes.

CONCLUSION

We compared the morphological, magnetic and adsorptive properties of iron oxide–silica nanocomposites prepared with different catalysts. The maximum crystallite size (11 nm) and best magnetization value (7 emu/g) was registered for M-HCl, which was chosen to test its ability to adsorb metal ions from aqueous solutions. The adsorption mechanism of Cr^{6+} and Zn^{2+} was studied by kinetic, thermodynamic and equilibrium studies. It was found that the adsorption process proceeds spontaneously, enhanced by the increase of temperature, being an endothermic process. The adsorption mechanism is best modelled according to the pseudo-second-order kinetic model. The equilibrium sorption data were modelled using Langmuir, Freundlich and Sips isotherms. The Sips isotherm was the one that best describes the mechanism of the adsorption for both Cr^{6+} and Zn^{2+}. The pHpzc of the M-HCl material was determined as being equal to 4 and with the increase of pH up to this value the adsorption capacity of the two ions increases up to pH=4, and then remains constant. The adsorption process was conducted at acidic pH, pH~4, where the adsorption mechanism of Cr^{6+} and Zn^{2+} can be described in four steps: (i) protonation of the active groups on the surface of the M-HCl material; (ii) adsorption of the metal ions on the protonated substrate and the metal ionic complexation; (iii) Cr^{6+} can be reduced by means of electron donor groups; and (iv) chemical complexation, electrostatic attraction or cation exchange processes are finally taking place [85,86]. All of the obtained nanocomposites presented higher adsorption affinity for Cr^{6+} ions. The highest adsorption capacity of ~30 mg/g for Cr^{6+} ions and ~6 mg/g for Zn^{2+} ions was for the samples prepared in the most acidic synthesis conditions.

ACKNOWLEDGEMENTS

The authors thank the Romanian Academy, the Inter-Academic Exchange Program between Romanian Academy and the Hungarian Academy of Sciences and for the scientific project and grant within the framework of scientific cooperation between Romania and JINR (Joint Institute for Nuclear Research) Dubna, Russia. Authors thank also Associate Professor Aurel Ercuța from West University of Timişoara, Romania, for magnetic measurements and fruitful discussions.

SUPPORTING INFORMATION

Additional information as noted in the text. This information is available via the Internet at http://www.springer.com/chemistry/journal/11814.

REFERENCES

1. P. B. Tchounwou, C. G. Yedjou, A. K. Patlolla and D. J. Sutton, in *Heavy metal toxicity and the environment*, A. Luch Eds., Molecular, Clinical and Environmental Toxicology. Experientia Supplementum, Springer, Basel (2012).
2. V. Bianchi, A. Zantedeschi, A. Montaldi and F. Majone, *Toxicol. Lett.*, **23**, 51 (1984).
3. S. Chen, Q. Yue, B. Gao, Q. Li and X. Xu, *Chem. Eng. J.*, **168**, 909 (2011).
4. S. Shariati, M. Khabazipour and F. Safa, *J. Porous Mater.*, **24**, 129 (2017).
5. T. Xia, M. Kovochich, M. Liong, L. Madler, B. Gilbert, H. Shi, J. I. Yeh, J. I. Zink and A. E. Nel, *ACS Nano*, **10**, 2121 (2008).
6. F. Fu and Q. Wang, *J. Enviror. Manage.*, **92**, 407 (2011).
7. M. K. Dinker and P. S. Kulkarni, *J. Chem. Eng. Data*, **60**, 2521 (2015).
8. P. P. Martin, M. F. Agosto, J. F. Bengoa and N. A. Fellenz, *J. Environ. Chem. Eng.*, **5**, 1210 (2017).
9. J. C. Almeida, C. E. D. Cardoso, D. S. Tavares, R. Freitas, T. Trindade, C. Vale and E. Pereira, *Trends Anal. Chem.*, **118**, 277 (2019).
10. K. Biswas, D. Bandhoyapadhyay and U. C. Ghosh, *Adsorption*, **13**, 83 (2007).
11. M. Alcala and C. Real, *Solid State Ion.*, **177**, 955 (2006).
12. S. Zhu, Y. Leng, M. Yan, X. Tuo, J. Yang, L. Almásy, Q. Tian, G. Sun, L. Zou, Q. Li, J. Courtois and H. Zhang, *Appl. Surf. Sci.*, **447**, 381 (2018).
13. W.-W. Wang and J.-L. Yao, *Mater. Lett.*, **64**, 840 (2010).
14. R. J. Desch, J. Kim and S. W. Thiel, *Micropor. Mesopor. Mater.*, **187**, 29 (2014).
15. P. N. R. Kishore and P. Jeevanandam, *J. Alloy. Compd.*, **522**, 51 (2012).
16. R. Nicola, O. Costişor, M. Ciopec, A. Negrea, R. Lazău, C. Ianăşi, E.-M. Picioruş, A. Len, L. Almásy, E. I. Szerb and A.-M. Putz, *Appl. Sci.*, **10**, 2726 (2020).
17. X. Zhang, T. Cheng, C. Chen, L. Wang, Q. Deng, G. Chen and C. Ye, *Mater. Res. Express*, **7**, 085007 (2020).
18. M. Bashir, S. Riaz and S. Naseem, *Mater. Today: Proceedings*, **2 B**, 5664 (2015).
19. A. Ercuta, *IEEE Trans. Instrum. Meas.*, **69**, 1643 (2020).
20. A. I. Kuklin, D. V. Soloviev, A. V. Rogachev, P. K. Utrobin, Yu. S. Kovalev, M. Balasoiu, O. I. Ivankov, A. P. Sirotin, T. N. Murugova, T. B. Petukhova, Yu. E. Gorshkova, R. V. Erhan, S. A. Kutuzov, A. G. Soloviev and V. I. Gordeliy, *J. Phys. Conf. Ser.*, **291**, 012013 (2011).
21. A. I. Kuklin, A. D. Rogov, Yu. E. Gorshkova, P. K. Utrobin, Yu. S. Kovalev, A. V. Rogachev, O. I. Ivankov, S. A. Kutuzov, D. V. Soloviov and V. I. Gordeliy, *Phys. Part. Nucl. Lett.*, **8**(2), 200 (2011).
22. A. I. Kuklin, A. Kh. Islamov and V. I. Gordeliy, *Neutron News*, **16**, 16 (2005).
23. M. Nyam-Osor, D. V. Soloviov, Yu. S. Kovalev, A. Zhigunov, A. V. Rogachev, O. I. Ivankov, R. V. Erhan and A. I. Kuklin, *J. Phys. Conf. Ser.*, **351**(1), 012024 (2012).
24. A. G. Soloviev, T. M. Solovjeva, O. I. Ivankov, D. V. Soloviov, A. V. Rogachev and A. I. Kuklin, *J. Phys. Conf. Ser.*, **848**(1), 012020 (2017).
25. P. Scherrer, *Nachr. Ges. Wiss. Gottingen*, **26**, 98 (1918).
26. Z. Dudás, E. Fagadar-Cosma, A. Len, L. Románszki, L. Almásy, B. Vlad-Oros, D. Dascălu, A. Krajnc, M. Kriechbaum and A. Kuncser, *Materials*, **11**(4), 565 (2018).
27. A.-M. Putz, A. Len, C. Ianasi, C. Savii and L. Almásy, *Korean J.*

Chem. Eng., **33**, 749 (2016).
28. N. N. Gubanova, A. Ye. Baranchikov, G. P. Kopitsa, L. Almásy, B. Angelov, A. D. Yapryntsev, L. Rosta and V. K. Ivanov, *Ultrason. Sonochem.*, **24**, 230 (2015).
29. C. Ianasi, O. Costisor, A.-M. Putz, R. Lazau, A. Negrea, D. Niznansky, L. Sacarescu and C. Savii, *Process. Appl. Ceram.*, **10**, 265 (2016).
30. A. Ercuta and M. Chirita, *J. Cryst. Growth*, **380**, 182 (2013).
31. M. Handa and H. Miyamoto, *Inorg. Chim. Acta*, **203**, 61 (1992).
32. Y. Yukawa, M. Handa and Y. Hoshino, *J. Solution Chem.*, **24**(1), 19 (1995).
33. Ph. Colomban and A. Slodczyk, *Acta Phys. Pol. A*, **116**, 7 (2009).
34. I. Diaz-Acosta, J. Baker, W. Cordes and P. Pulay, *J. Phys. Chem. A*, **105**, 238 (2001).
35. U. A. Jayasooriya, J. N. T. Peck, J. E. Barclay, S. M. Hardy, A. I. Chumakov, D. J. Evans, C. J. Peakett and V. S. Oganesyan, *Chem. Phys. Lett.*, **518**, 119 (2011).
36. I. Pavel, A. Szeghalmi, D. Moigno, S. Cinta and W. Kiefer, *Biopolymers*, **72**(1), 25 (2003).
37. T. F. Tirrell, M. L. Paddock, A. R. Conlan, E. J. Smoll Jr., R. Nechushtai, P. A. Jennings and J. E. Kim, *Biochemistry*, **48**(22), 4747 (2009).
38. M. Thommes, K. Kaneko, A. V. Neimark, J. P. Olivier, F. Rodriguez-Reinoso, J. Rouquerol and K. S. W. Sing, *Pure Appl. Chem.*, **87**, 1051 (2015).
39. C. Ianăşi, M. Picioruş, R. Nicola, M. Ciopec, A. Negrea, D. Nižňanský, A. Len, L. Almásy and A.-M. Putz, *Korean J. Chem. Eng.*, **36**, 688 (2019).
40. M. Kosmulski, *Surface charging and points of zero charge, engineering and technology, Physical Sciences*, CRC Press, Boca Raton (2009).
41. K. Mulani, S. Daniels, K. Rajdeo, S. Tambe and N. Chavan, *J. Polym.*, **2013**, Article ID 798368 (2013).
42. Y. S. Ho, *J. Hazard. Mater.*, **136**, 681 (2006).
43. M. Yurdakoc, Y. Seki, S. Karahan and K. Yurdakoc, *J. Colloid Interface Sci.*, **286**, 440 (2005).
44. Y Zhang, F. Yu, W. Cheng, J. Wang and J. Ma, *J. Chem.*, **2017**, Article ID 1936829 (2017).
45. R. Abraham, S. Mathew, S. Kurian, M. P. Saravanakumar, A. M. Ealias and G. George, *Ultrason. Sonochem.*, **49**, 175 (2018).
46. K. Vijayaraghavan, J. Mao and Y. S. Yun, *Bioresour. Technol.*, **99**, 2864 (2008).
47. M. U. Dural, L. Cavas, S. K. Papageorgiou and F. K. Katsaros, *Chem. Eng. J.*, **168**, 77 (2011).
48. D. Do Duong, *Adsorption analysis: Equilibria and kinetics, series on chemical engineering*, vol. 2, Imperial College Press, London (1998).
49. Z. Ren, X. Xu, X. Wang, B. Gao, Q. Yue, W. Song, L. Zhang and H. Wang, *J. Colloid Interface Sci.*, **468**, 313 (2016).
50. K. Handore, S. Bhavsar, A. Horne, P. Chhattise, K. Mohite, J. Ambekar, N. Pande and V. Chabukswar, *J. Macromol. Sci. A*, **51**, 941 (2014).
51. S. R. Chowdhury, E. K. Yanful and A. R. Pratt, *J. Hazard. Mater.*, **235-236**, 246 (2012).
52. A. Kelly and K. M. Knowles, *Crystallography and crystal defects*, 2nd Ed., Wiley, United Kingdom (2012).
53. J. C. Igwe and A. A. Abia, *Eclética Química*, **32**(1), 33 (2007).
54. V. Kavelin, O. Fesenko, H. Dubyna, C. Vidal, T. A. Klar, C. Hrelescu and L. Dolgov, *Nanoscale Res. Lett.*, **12**, 197 (2017).
55. B. K. Mohapatra and D. V. R. Rao, *Z. Anorg. Allg. Chem.*, **372**(3), 332 (1970).
56. M. Windholz, The Merck Index, 9th Ed., vol. 802, Merck & Company, Whitehouse Station, NJ, USA (1976).
57. A. M. Ealias and M. P. Saravanakumar, *J. Environ. Manage.*, **206**, 215 (2018).
58. R. Bhatt, B. Sreedhar and P. Padmaja, *Int. J. Biol. Macromol.*, **104**, 1254 (2017).
59. H. Gao, Y. Liu, G. Zeng, W. Xu, T. Li and W. Xia, *J. Hazard. Mater.*, **150**, 446 (2008).
60. G. Burillo, J. Serrano-Gomez and J. Bonifacio-Martinez, *J. Mexican Chem. Soc.*, **57**, 80 (2013).
61. M. Gheju, I. Balcu and G. Mosoarca, *J. Hazard. Mater.*, **310**, 270 (2016).
62. A. Aliyu, *Scientific African*, **3**, e00069 (2019).
63. S. Mnasri-Ghnimi and N. Frini-Srasra, *Appl. Clay Sci.*, **158**, 150 (2018).
64. Renu, Madhu Agarwal and K. Singh, *J. Water Reuse Desal.*, **7**(4), 387 (2016).
65. L. B. Tahar, M. H. Oueslati and M. J. A. Abualreish, *J. Colloid Interface Sci.*, **512**, 115 (2018).
66. S. Shi, J. Yang, S. Liang, M. Li, Q. Gan, K. Xiao and J. Hu, *Sci. Total. Environ.*, **628-629**, 499 (2018).
67. Y. Li, S. Zhu, Q. Liu, Z. Chen, J. Gu, C. Zhu, T. Lu, D. Zhang and J. Ma, *Water Res.*, **47**, 4188 (2013).
68. C. Wan and J. Li, *ACS Sustain. Chem. Eng.*, **3**, 2142 (2015).
69. V. Srivastava and Y. C. Sharma, *Water Air Soil Pollut.*, **225**, 1 (2013).
70. J. Hu, G. H. Chen and I. M. C. Lo, *Water Res.*, **39**, 4528 (2005).
71. P. Wang and I. M. C. Lo, *Water Res.*, **43**, 3727 (2009).
72. W. Jiang, M. Pelaez, D. D. Dionysiou, M. H. Entezari, D. Tsoutsou and K. O'Shea, *Chem. Eng. J.*, **222**, 527 (2013).
73. B. N. Mahato and T. Krithiga, *Mater Today: Proc.*, **17**, 303 (2019).
74. R. Ullah, B. K. Deb and M. Y. A. Mollah, *Defect Diffus. Forum*, **353**, 33 (2014).
75. J. Zhang, S. Lin, M. Han, Q. Su, L. Xia and Z. Hui, *Water*, **12**, 446 (2020).
76. J. Wei, Z. Yang, Y. Sun, C. Wang, J. Fan, G. Kang, R. Zhang, X. Dong and Y. Li, *J. Mater. Sci.*, **54**, 6709 (2019).
77. M. Xing, Q. Xie, X. Li, T. Guan and D. Wu, *Environ. Technol.*, **41**(5), 658 (2020).
78. A. Ahmadi, S. Heidarzadeh, A. R. Mokhtari, E. Darezereshki and H. A. Harouni, *J. Geochem. Explor.*, **147**, 151 (2014).
79. L. Yuan and Y. Liu, *Chem. Eng.*, **432**, 215, (2013).
80. E. Matei, A. M. Predescu, G. Coman, M. Bălănescu, M. Sohaciu, C. Predescu, L. Favier and M. Niculescu, *Environ. Eng. Manag. J.*, **15**, 1019 (2016).
81. B. C. Nyamunda, T. Chivhanga, U. Guyo and F. Chigondo, *J. Eng.*, **2019**, Art. ID. 5656983 (2019).
82. A. Roy and J. Bhattacharya, *Chem. Eng.*, **211-212**, 493 (2012).
83. A. M. Ealias and M. P. Saravanakumar, *Environ. Sci. Pollut. Res.*, **27**, 2955 (2020).
84. G. George and M. P. Saravanakumar, *Environ. Sci. Pollut. Res.*, **25**, 30236 (2018).
85. Y.-J. Zhang, J.-L. Ou, Z.-K. Duan, Z.-J. Xing and Y. Wang, *Colloids Surf. A*, **481**, 108 (2015).
86. M. A. Islam, M. J. Angove and D. W. Morton, *Environ. Nanotechnol. Monit. Manag.*, **12**, 100267 (2019).

Supporting Information

Effects of catalysts on structural and adsorptive properties of iron oxide-silica nanocomposites

Cătălin Ianăși*, Paula Ianăși (b. Svera),***, Adina Negrea****,†, Mihaela Ciopec****, Oleksandr I. Ivankov*****,******,*******, Alexander I. Kuklin*****,******, László Almásy********, and Ana-Maria Putz*,†**

*"Coriolan Drăgulescu" Institute of Chemistry, 24th Mihai Viteazul Bvd., 300223, Timişoara, România
**National Institute for Research and Development in Electrochemistry and Condensed Matter, 144th Prof. Dr. Aurel Paunescu-Podeanu Street, 300569, Timişoara, România
***Department of Biology-Chemistry, Faculty of Chemistry, Biology, Geography, West University of Timişoara, Pestalozzi Str. No. 16, RO-300115, Timişoara, România
****Politechnica University of Timişoara, Faculty of Industrial Chemistry and Environmental Engineering, 6th Vasile Pârvan Bvd., 300223, Timişoara, România
*****Frank Laboratory of Neutron Physics, Joint Institute for Nuclear Research, Joliot-Curie 6, Dubna, Russia
******Research Center for Molecular Mechanisms of Aging and Age-Related Diseases, Moscow Institute of Physics and Technology, 141701 Dolgoprudny, Russia
*******Institute for Safety Problems of Nuclear Power Plants NAS of Ukraine, 03028 Kyiv, Ukraine
********Institute for Energy Security and Environmental Safety, Centre for Energy Research, Konkoly-Thege str. 29-33, 1121 Budapest, Hungary
(*Received 11 May 2020 • Revised 16 August 2020 • Accepted 6 September 2020*)

SEM Analysis

Scanning electron microscopy (SEM) before and after adsorption were done in order to investigate the interactions between chromium and zinc ions with the surfaces of the materials and were

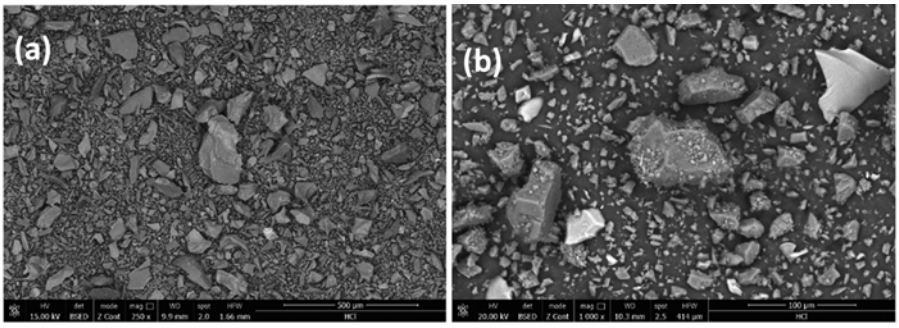

M-HCl sample at 250x(left) and 1000x(right)

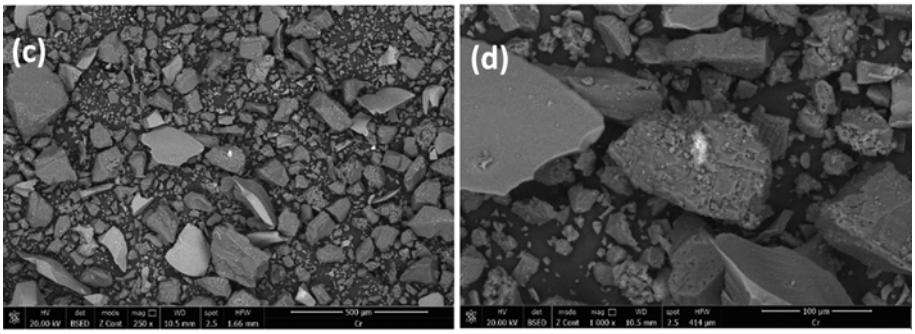

M-HCl sample after adsorption for Cr, at 250x(left) and 1000x(right)

Fig. S1. Scanning electron microscopy (SEM) before and after adsorption.

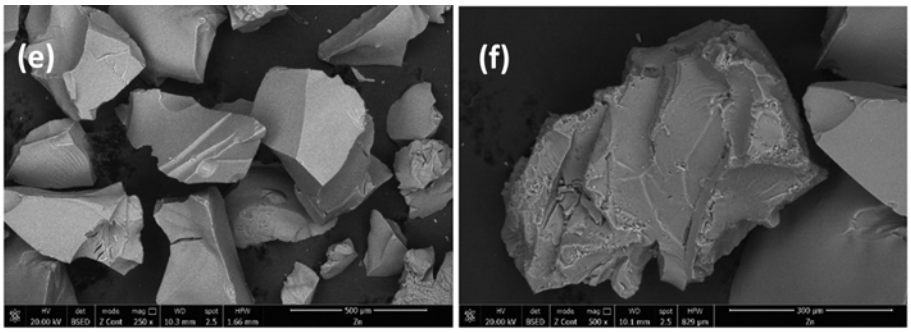

M-HCl sample after adsorption for Zn, at 250x(left) and 1000x(right)

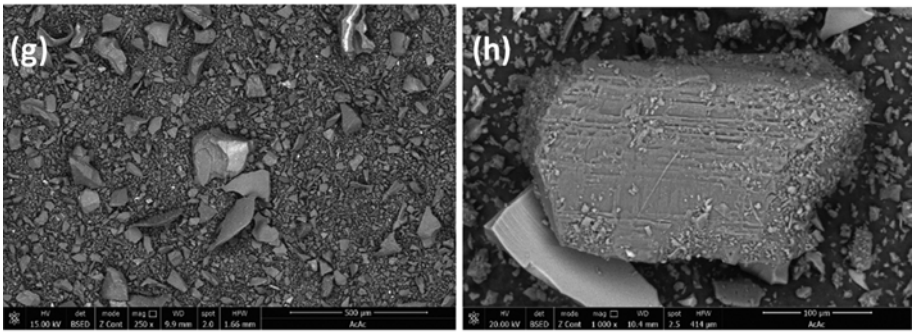

M-CH3COOH sample at 250x(left) and 1000x(right)

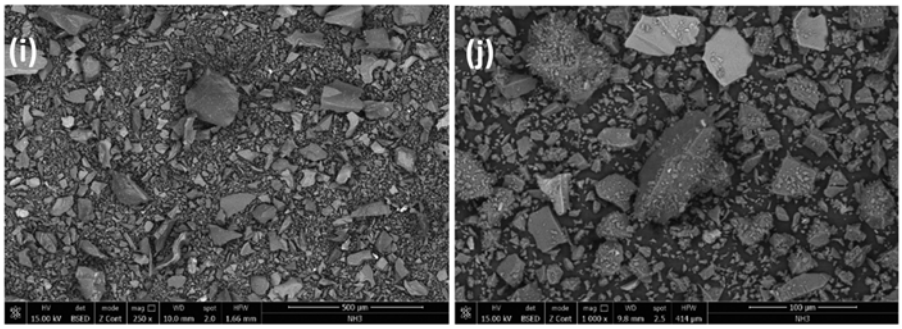

M-NH3 sample at 250x(left) and 1000x(right)

Fig. S1. Continued.

presented in Fig. S1.

It can be seen that the adsorbent material before the adsorption of metal ions has a fine powdery morphology, with relatively small pore sizes, and after adsorption, the material agglomerated as blocks, which can confirm that metal ions in anionic form such as chromate $[CrO_4]^{2-}$, dichromate $[Cr_2O_7]^{2-}$ or hydrogen chromate $[HCrO_4]^-$. In the case of zinc, adsorption can be achieved by Si-O-Zn bonds that extend the network. In the crystalline network of SiO_2, there are Si-O-Si bonds, but there is also O in the form of OH. This H allows the formation of Si-O-Zn bonds. These arguments can be supported by the disappearance of OH groups from the FT-IR spectrum and appearance of Si-O-Zn bonds.